

A Trinocular Vision Probe for Sculptured Surface Measurements

G.X. Zhang, H.W. Zhang, Z. Liu, J.B. Guo, X. S. Zhao, Y.M. Fan, Z.R. Qiu, X.F. Li, Z. Li
 State Key Laboratory of Precision Measuring Technology and Instruments,
 Tianjin University, Tianjin 300072, China

Keywords: Sculptured surface measurement; trinocular vision probe; camera calibration; matching technique; reconstruction

1. Introduction

Reverse engineering of free-form surfaces is one of the most challenging technologies in advanced manufacturing [1]. With the development of industry more and more sculptured surfaces, such as molds and dies, turbine blades, are required to measure quickly and accurately. Optical non-contact probes possess many advantages, such as high speed, no measuring force, no deformation caused, in comparison with contact ones [2]. The ability of stereo vision probe with CCD cameras in gathering a large amount of information simultaneously makes it the most popularly used one in sculptured surface measurements. As a common practice two CCD cameras are used to form a binocular system and the geometric features of the object are obtained by matching two images captured by these cameras. The following deficiencies were discovered in such a system [3]. A mismatch might occur when certain part of the object is hidden by some obstacles or the images are blurred or noisy. Mismatches also might happen in case of having repeating sceneries or little change in the grey level of sceneries. The accuracy of measurement is deteriorated when the angle formed by the measured curve and epipolar line used for image matching is small. To overcome all these problems a line structured light trinocular vision probe for sculptured surface measurements is developed. It distinguishes itself by high efficiency, high accuracy and reliability, as well as applicability for on-line measurement of complicated sculptured surfaces.

2. Working Principle

The working principle of the trinocular vision probe is shown in Figure 1. A light stripe emitted from the laser head is projected on the surface measured. The light stripe is deformed in accordance with the form of sculptured surface. Three CCD cameras are used to capture the images of the deformed light stripe. The form and the position of the surface are determined by matching these images. The main trouble in measuring high-reflective sculptured surfaces is that the specular light is much stronger than the diffused one. Two images might be formed in each CCD camera. One is formed by the specular light, another by diffused light. For solving this problem a polarizer and three analyzers are used. The light stripe projected on the surface is linearly polarized. The specular light will be also linearly polarized whereas diffused light forms a polarization ellipsoid. The polarization directions of the analyzers are perpendicular to that of polarizer. The specular light is eliminated in large degree and only the diffused light can reach three CCD cameras.

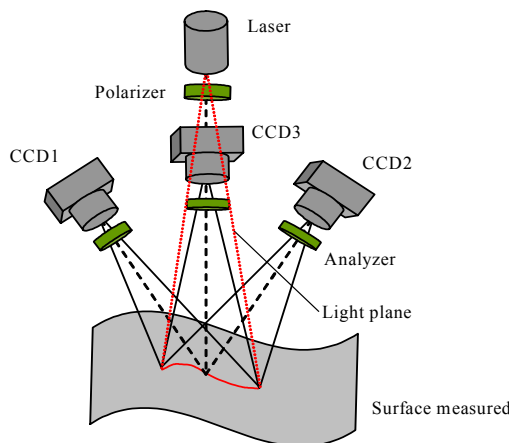


Figure 1 Diagram of the trinocular probe

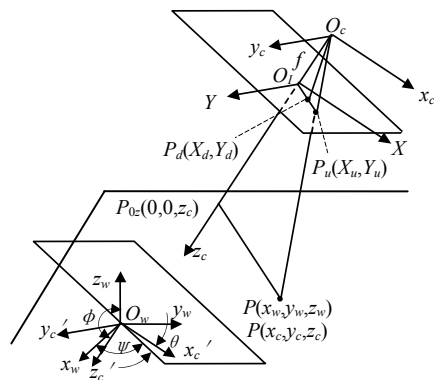


Figure 2 Coordinate transformation between camera and workpiece systems

3. System optimization

In Figure 2 only one camera is shown. $O_w x_w y_w z_w$ is the workpiece system and $O_c x_c y_c z_c$ is the camera system. The coordinate transformation relations between two systems can be expressed as

$$\begin{bmatrix} x_c \\ y_c \\ z_c \end{bmatrix} = R \begin{bmatrix} x_w \\ y_w \\ z_w \end{bmatrix} + T \quad \text{OR} \quad \begin{bmatrix} x_w \\ y_w \\ z_w \end{bmatrix} = R' \begin{bmatrix} x_c \\ y_c \\ z_c \end{bmatrix} + T' \quad (1)$$

$$\text{and } R = \begin{bmatrix} r_1 & r_2 & r_3 \\ r_4 & r_5 & r_6 \\ r_7 & r_8 & r_9 \end{bmatrix}, \quad R' = R^{-1} = \begin{bmatrix} r'_1 & r'_2 & r'_3 \\ r'_4 & r'_5 & r'_6 \\ r'_7 & r'_8 & r'_9 \end{bmatrix}, \quad T = \begin{bmatrix} T_x \\ T_y \\ T_z \end{bmatrix}, \quad T' = \begin{bmatrix} T'_x \\ T'_y \\ T'_z \end{bmatrix} \quad (2)$$

where R and R' are rotational matrices, T and T' are translation matrices. All components r_i and r'_i ($i=1\sim 9$) in R and R' are functions of three Euler angles ϕ, ψ, θ . From perspective imagery it can be derived

$$X = f \frac{x_c}{z_c}, \quad Y = f \frac{y_c}{z_c} \quad (3)$$

where X and Y are coordinates of a point on the image plane and f is the camera constant. From (1), (2) and (3)

$$x_w = \frac{(y_w - T'_y)(r'_1 X + r'_2 Y + r'_3 f)}{r'_4 X + r'_5 Y + r'_6 f} + T'_x \quad \text{and} \quad z_w = \frac{(y_w - T'_y)(r'_7 X + r'_8 Y + r'_9 f)}{r'_4 X + r'_5 Y + r'_6 f} + T'_z \quad (4)$$

Both x_w and z_w are functions of $(X, Y, \phi, \psi, \theta, f, T'_x, T'_y, T'_z)$. By taking partial derivatives it can be calculated

$$\Delta z_w = \frac{|f(T'_y - y_w)|}{(Y \cos \phi + f \sin \phi)^2} |\Delta Y| = \frac{f(T'_y - y_w)}{(f^2 + Y^2) \sin^2(\phi + \tan^{-1} \frac{Y}{f})} |\Delta Y| \quad (5)$$

In discussion of the optimal arrangement it is reasonable to assume $Y=0$ when $y_w=0$ and the optical axis of the camera passes through point O_w . In this case $T'_y = T'_z \tan \phi$ when $\theta = \psi = 0$, and Formula (5) takes form

$$\Delta z_w = \frac{2fT'_z}{f^2 \sin 2\phi} |\Delta Y| \quad (6)$$

Δz_w gets its minimum under fixed ΔY when $\phi = \pi/4$. However the larger the ϕ the larger the dimension of the probe. For reducing the dimension of the probe $\phi = \pi/6$ is taken in our design. Three CCD cameras form a regular triangle as shown in Figure 3a. 2α is the view angle of the camera. The common zone of view is shown by shadow area in Figure 3b and

$$\delta = 2\gamma = 2(\pi/2 - \sigma) = \pi - 2 \tan^{-1} \left(\frac{\sqrt{3}t}{2d'} \right) = \pi - 2 \tan^{-1} \left(\frac{\sqrt{3}t}{2\sqrt{d^2 + (t/2)^2}} \right) \approx \pi - 2 \tan^{-1} \frac{B}{2d} \quad (7)$$

where d is the object distance. The common view zone increases with the increase of object distance d and decrease of base line length B . After calculation it can be also shown the depth of field increases with the increases of focal

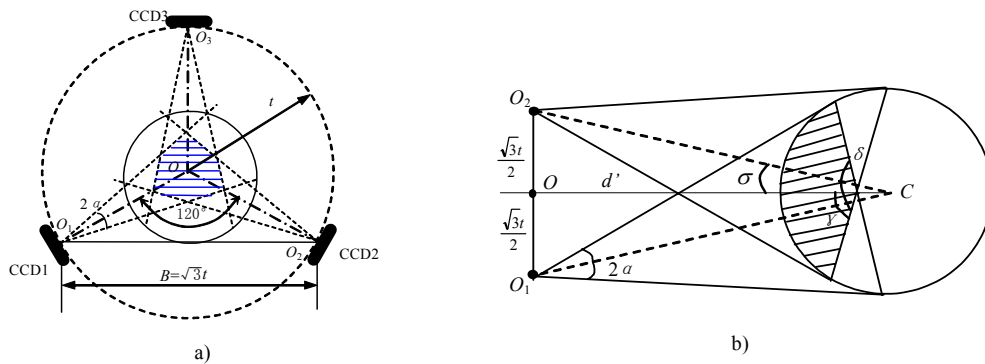


Figure 3 View area of the probe

length, and the decreases of magnification factor, numerical aperture, and diameter of the incident pupil. All these factors should be considered simultaneously and some compromises should be made in the probe design.

4. Camera calibration

In order to obtain the corresponding relationship between the positions of the points in space and the pixel numbers in the images camera calibration is essential. In the current time Tsai's two step method [4] is the most popularly used method among techniques for calibrating camera parameters. This method determines most of the camera parameters including camera constant f , coordinates of the image center (C_x, C_y) , lens distortion coefficient k and position of the camera with reference to the artifact, based on the radial alignment constraint by using nonlinear searching. But this method cannot determine the uncertainty of the scale factor in horizontal direction s_x . For solving this problem a technique based on a virtual 3-D artifact shown in Figure 4 is proposed in this paper.

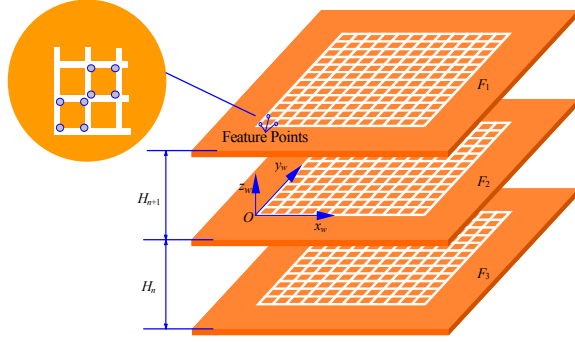


Figure 4 3-D virtual artifact

Since 3D artifact is difficult to make a 2D artifact in form of a grid plate is applied in our study. The grid plate is mounted at different heights during the calibration process to form a virtual 3D artifact. The following equations can be written.

$$\left. \begin{aligned} X'_{di} &= X_{di} s_x = (X_{fi} - C_x) d'_x \\ Y_{di} &= (Y_{fi} - C_y) d_y \\ d'_x &= d_x N_{cx} / N_{fx} \end{aligned} \right\} \quad (8)$$

where (X_{fi}, Y_{fi}) are coordinates of i -th image point in pixels; (C_x, C_y) are coordinates of the image center in pixels; d_x and d_y are pixel intervals in x and y directions, respectively; N_{cx} and N_{fx} are number of the pixels on the CCD element and number of points sampled

by the graphic card in horizontal direction, respectively. (X_{di}, Y_{di}) and (X_{ui}, Y_{ui}) are coordinates of the distorted and undistorted images of i -th feature point in millimeters, respectively. From (1), (2), (3) and (8) we have

$$\frac{X'_d}{Y_d} = \frac{X_u}{Y_u} = \frac{x_c}{y_c} = \frac{r_1 x_w + r_2 y_w + r_3 z_w + T_x}{r_4 x_w + r_5 y_w + r_6 z_w + T_y} \quad (9)$$

$$\text{or } \begin{bmatrix} Y_{di} x_{wi} & Y_{di} y_{wi} & Y_{di} z_{wi} & Y_{di} & -X'_{di} x_{wi} & -X'_{di} y_{wi} & -X'_{di} z_{wi} \end{bmatrix} L' = X'_{di} \quad (10)$$

$$L' = [a_1 \ a_2 \ a_3 \ a_4 \ a_5 \ a_6 \ a_7]^T = [T_y^{-1} s_x r_1 \ T_y^{-1} s_x r_2 \ T_y^{-1} s_x r_3 \ T_y^{-1} s_x T_x \ T_y^{-1} r_4 \ T_y^{-1} r_5 \ T_y^{-1} r_6]^T \quad (11)$$

In Formula (10) $i=1 \sim N$, N is the total number of calibrated points. All values except (C_x, C_y) are obtained from calibration measurement. The coordinates of the center of computer frame memory are taken as the initial values of (C_x, C_y) . L' can be determined by least square fitting. Since $r_1^2 + r_2^2 + r_3^2 = 1$ and $r_4^2 + r_5^2 + r_6^2 = 1$, we obtain

$$|T_y| = (a_5^2 + a_6^2 + a_7^2)^{-1/2} \quad \text{and} \quad s_x = (a_1^2 + a_2^2 + a_3^2)^{1/2} |T_y| \quad (12)$$

After s_x has been obtained Tsai's two step method can be applied to calibrate all the intrinsic and extrinsic parameters of the camera. For improving the accuracy of calibration iterations are often required.

5. Sampling strategy

Sampling strategy is important to obtain all the required data with high accuracy in a short time. The first problem here is selecting the correct scanning direction. There are two types of machined surfaces. Ground and lapped surfaces belong to the first type. There is almost no visible machined trace in certain direction. However the machined traces might be quite obvious for turned, milled and planed surfaces. In the later cases it is recommended to arrange the light stripe in the direction perpendicular to the machined traces as shown in Figure 5a and a straight line image shown in Figure 5b is obtained. When the light stripe is in the direction parallel to the machined traces as shown in Figure 5c a bright spot shown in Figure 5d might be formed.

The next question is selecting the step in scanning. An adaptive sampling strategy based on the curvature of surface in the scanning direction is developed. The step distance is determined by $S = \sqrt{8\rho h}$, where ρ is the radius of curvature and h is the allowed chord height in each sampling interval. Similar idea is applied to the data point sampled on each light stripe.

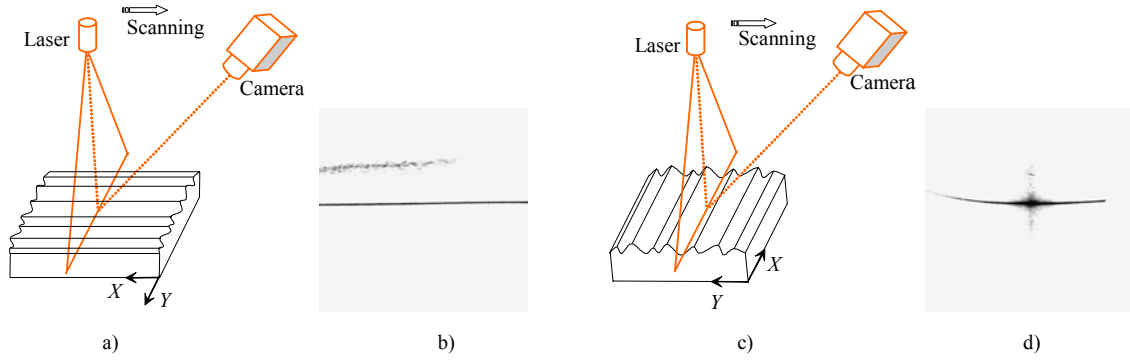


Figure 5 Scanning directions

6. Feature extraction

The image of the line stripe is a zone with certain grey distribution. The position of the extracted feature depends in large degree on the chosen threshold. The grey level $f(i, j)$ of the image at point (i, j) depends not only on the position of the point but also a lot of other factors, such as illumination, shadow, background and neighborhood grey levels. The threshold should be adaptive to these factors. A threshold technique based on the grey transition region is used in our study [5]. The effective average gradient of EAG is defined as

$$EAG = TG/TP \quad \text{and} \quad TG = \sum_{i,j \in Z} g(i, j), \quad TP = \sum_{i,j \in Z} p(i, j) \quad (13)$$

where $i, j \in Z$ means that the integrals are taken for the whole zone. $g(i, j)$ is the gradient of grey level. $g(i, j) = \sqrt{\Delta_x f(i, j)^2 + \Delta_y f(i, j)^2}$ and $\Delta_x f(i, j) = f(i, j) - f(i-1, j)$, $\Delta_y f(i, j) = f(i, j) - f(i, j-1)$ and $p(i, j) = 1$ when $g(i, j) > 0$, $p(i, j) = 0$ when $g(i, j) = 0$.

High cut grey level $f_{high}(i, j)$ is defined as $f_{high}(i, j) = Q_h$ when $f(i, j) \geq Q_h$; and $f_{high}(i, j) = f(i, j)$ when $f(i, j) < Q_h$. Low cut grey level $f_{low}(i, j)$ is defined as $f_{low}(i, j) = Q_l$ when $f(i, j) \leq Q_l$; and $f_{low}(i, j) = f(i, j)$ when $f(i, j) > Q_l$.

It is obvious the values of $EAG_{high}(Q_h)$ and $EAG_{low}(Q_l)$ depend on the values of Q_h and Q_l chosen. The values of Q_h and Q_l under which $EAG_{high}(Q_h)$ and $EAG_{low}(Q_l)$ reach their maximums are expressed by Q_{high} and Q_{low} and define the transition zone as shown in Figure 6. The average value of the grey level within this transition zone is defined as the threshold for feature extraction.

For enhancing the accuracy of feature extraction a sub-pixel edge detection algorithm based on the spatial moment theory is adopted in our work [6]. The position of the sub-pixel edge l can be calculated from

$$l = \frac{4M'_{20} - M_{00}}{3M'_{10}} \quad (14)$$

where: $M'_{10} = \sqrt{M^2_{01} + M^2_{10}}$, $M'_{20} = \frac{M^2_{10}M_{20} + 2M_{01}M_{10}M_{11} + M^2_{01}M_{02}}{M^2_{01} + M^2_{10}}$, $M_{pq} = \iint x^p y^q f(x, y) dx dy$.

7. Image matching

The position of a feature point in space cannot be determined just by its image in one camera. Image matching is an important step for determining the position of a feature point in space. For improving the accuracy and reliability of image matching both geometric constraints and grey level similarity constraint are applied. The geometric constraints include following three statements: (1) Uniqueness: Each point has a unique image point on the image plane. (2) Projection constraint: Each point on the image plane might correspond to different points in the space. However all they lie on the line connecting the optical center of the camera and the image point. (3) Light stripe constraint: The point in space must lie on the light stripe, which generates the image.

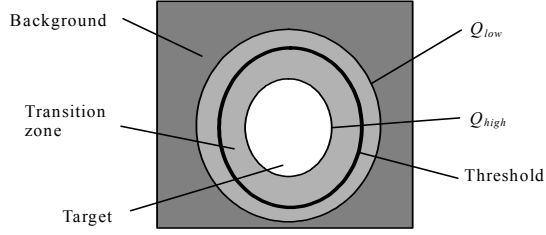


Figure 6 Transition zone

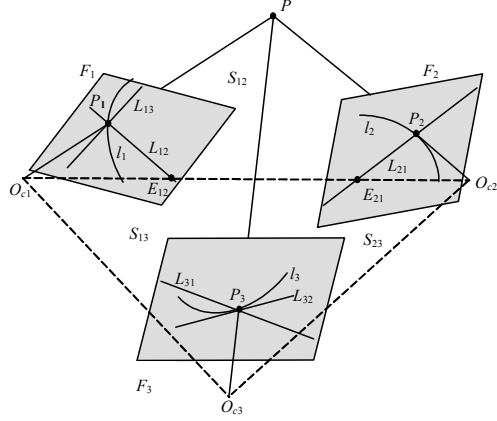


Figure 7 Image matching

In Figure 7 O_{ci} ($i=1\sim 3$) are optical centers of three cameras. F_i is the image plane of camera i . l_i is the image of line stripe on image plane F_i . P_i is the projection of point P on F_i , which is the intersection point of PO_{ci} and F_i . P_1 , P_2 and P_3 are called homologous images. The plane formed by $PO_{ci}O_{cj}$ ($j=1\sim 3, j \neq i$) is called epipolar plane S_{ij} . Intersection of epipolar plane S_{ij} with plane F_i forms epipolar line L_{ij} . L_{ij} and L_{ji} are called conjugation epipolar lines. E_{ij} is the intersection point of the optical center line $O_{ci}O_{cj}$ with image plane F_i and called epipole. The homologous image P_2 of image P_1 on plane F_2 must be on epipolar line L_{21} . Form another side it should be on image of line stripe l_2 . So it must be located at the intersection point P_2 of L_{21} and l_2 as shown in Figure 7. The homologous image P_3 of image P_1 on plane F_3 must be on epipolar line L_{31} . Form another side it should be on image of line stripe l_3 . So it must be located at the intersection point P_3 of L_{31} and l_3 . In the mean time it should be also located on epipolar line L_{32} . Since all the images are subject to have certain errors for improving the accuracy and reliability of image matching the grey level similarity constraint is applied simultaneously. The grey level similarity of points P_1 , P_2 and P_3 is evaluated according to the following formulas [7]. First the average $\overline{f_i(u_i, v_i)}$ and standard deviation $\sigma(f_i)$ of the grey level of point P_i in a neighborhood area with $(2N+1) \times ((2M+1)$ pixels are calculated.

$$\overline{f_i(u_i, v_i)} = \frac{\sum_{n=-N}^N \sum_{m=-M}^M f_i(u_{i+n}, v_{i+m})}{(2N+1)(2M+1)}, \quad \sigma(f_i) = \sqrt{\frac{\sum_{n=-N}^N \sum_{m=-M}^M f_i^2(u_{i+n}, v_{i+m})}{4NM} - \overline{f_i^2(u_i, v_i)}} \quad (15)$$

After that the correlation between the grey levels of points P_i and P_j $\text{Cor}(P_i, P_j)$ and similarity of three points $\text{Similarity}(P_1, P_2, P_3)$ are calculated.

$$\text{Cor}(P_i, P_j) = \frac{\sum_{n=-N}^N \sum_{m=-M}^M [f_i(u_{i+n}, v_{i+m}) - \overline{f_i(u_i, v_i)}] \times [f_j(u_{j+n}, v_{j+m}) - \overline{f_j(u_j, v_j)}]}{4NM \sigma(f_i) \sigma(f_j)} \quad (16)$$

$$\text{Similarity}(P_1, P_2, P_3) = \frac{1}{3} \text{Cor}(P_1, P_2) + \frac{1}{3} \text{Cor}(P_1, P_3) + \frac{1}{3} \text{Cor}(P_2, P_3) \quad (17)$$

The homologous images are searched in a defined neighborhood of points P_2 and P_3 .

Based on any two of homologous images among P_1 , P_2 and P_3 a point P_{ij} in space can be determined. The gravity center of the triangle form by P_{12} , P_{13} and P_{23} is taken as the position of point P .

8. Data reconstruction

Due to huge amount of sampled data a data reduction algorithm based on distance criterion is applied before data reconstruction [8]. A straight line is formed by two end points P_1 and P_n of the light stripe after image processing. A point P_m with maximum departure from line P_1P_n is found and distance δ from P_m to line P_1P_n is calculated. All points between P_1 and P_n will be ignored and replaced by a straight line P_1P_n if $\delta < \delta_0$, where δ_0 is the given

threshold. P_m will be kept for further data processing if $\delta > \delta_0$, and P_m will be used as the new end point. Two straight lines P_1P_m and P_mP_n are formed. The whole process repeats until all points on the line stripe will be processed.

Since only the NURBS meets the requirement defined by STEP and is applicable for reverse engineering an algorithm combining triangular Bezier patch modeling technique with NURBS modeling technique is developed. All the data points are projected to $x_wO_wy_w$ plane of the world coordinate system. There is a correspondence between point in space and projected point in case of monotonic convex or concave sculptured surface. The Delaunay triangular division and Bezier interpolation are applied to get a G^0 continuous Bezier surface. The projection of the reconstructed Bezier surface on $x_wO_wy_w$ plane is divided into grids to meet the requirement of NURBS modeling. NURBS interpolation is applied to get a G^2 continuous surface. Smoothing is carried out by adjusting the controlling points.

9. Experiments

For verifying the accuracy and feasibility of the developed probe some gage blocks, a cylinder and a turbine blade surface were measured. Experiments show that the trinocular probe enhances both accuracy and reliability of measurement in comparison with binocular one. An accuracy of 0.02 mm was achieved in the first prototype developed. Some data of gage block measurements are given in Table 1. The standard deviation in measuring a cylinder is 0.01mm.

Table 1 Results of gage block measurement

No. of gauge block surface	Nominal height of the block from the base surface (mm)	Measured height of the block from the base surface (mm)	Deviation from nominal value (mm)
1	2	1.9971	-0.0029
2	3	2.9922	-0.0078
3	5	4.9893	-0.0107

10. Acknowledgements

This study is financially supported by the National Natural Science Foundation of China (project No.50075064) and Ronghong Endowment of the United Technologies Corporation, USA. The authors would like to express their sincere appreciation to the National Natural Science Foundation of China and Ronghong Endowment of USA.

11. References

- [1] Werner A, et al. Reverse Engineering of Free-form Surface. Journal of Material Processing Technology, 1998, 76: 128~132
- [2] Saito K, et al. Non-contact 3-D Digitizing and Machining System for Free-form Surface. Annals of CIRP, 1991, 40 (1): 483~486
- [3] Umesh R D, Aggarwal J K. Binocular versus Trinocular Stereo. IEEE Intelligence Transportation Systems Conference Proceedings, 1990, (1):2045~2050
- [4] Tsai R Y. A Versatile Camera Calibration Technique for High-Accuracy 3D Machine Vision Metrology Using Off-the-Shelf TV Cameras and Lenses. IEEE Journal of Robotics and Automation, 1987, RA-3(4):323-344
- [5] Castleman K R. Digital Image processing, 1998, Prentice-Hall International, Inc.
- [6] Edward P L, Owen R. Subpixel Measurements Using a Moment-Based Edge Operator. IEEE Transactions on Pattern Analysis and Matching Intelligence, 1989, 11(12): 1293~1309
- [7] Elsayed E H. A 3-D Trinocular Active Vision System for Surface Reconstruction. PhD Thesis, 1992, University of Cairo
- [8] Chen Y H, Ng C T, Wang Y Z. Data Reduction in Integrated Reverse Engineering and Rapid Prototyping. International Journal of Computer Integrated Manufacturing, 1999, 12(2):97-103